Crystallization of $RE_2(OH)_2CO_3SO_4{\cdot}nH_2O$ as a new family of layered hydroxides (RE = Gd−Lu lanthanides and Y), derivation of $RE_2O_2SO_4$, photoluminescence and optical thermometry

Fan Li[a], Zhenqi Song[a], Zhiyuan Pan[a], Sihan Feng[a], Qi Zhu[a], Ji-Guang Li[b,*]

[a] *Key Laboratory for Anisotropy and Texture of Materials (Ministry of Education), School of Materials Science and Engineering, Northeastern University, Shenyang, Liaoning, 110819, China*

[b] *Research Center for Functional Materials, National Institute for Materials Science, Tsukuba, Ibaraki, 305-0044, Japan*

[*]Corresponding author

Dr. Ji-Guang Li

National Institute for Materials Science

Tel: +81-29-860-4394

E-mail: li.jiguang@nims.go.jp

Abstract

Layered rare-earth hydroxides (LREHs) draw wide research interest because of their peculiar crystal structure, rich interlayer chemistry and abundant functionality of the RE element, but are limited to the two categories of $RE_2(OH)_5A{\cdot}nH_2O$ (A: typical of Cl^- or NO_3^-) and $RE_2(OH)_4SO_4{\cdot}nH_2O$. On the other hand, $RE_2O_2SO_4$ attracted attention for large-capacity oxygen storage, low-temperature magnetism and luminescence, whose preparation mostly involves toxic SO_x gases and/or complicated procedures. This study produced $RE_2(OH)_2CO_3SO_4{\cdot}nH_2O$ as a new family of LREHs (RE = Gd-Lu lanthanides and Y) via hydrothermal reaction, from which phase-pure $RE_2O_2SO_4$ was derived via subsequent annealing at 800 °C in air without the involvement of SO_x. The compounds were thoroughly characterized to reveal the intrinsic influence of lanthanide contraction (RE^{3+} radius) on crystal structure, thermal behavior (dehydroxylation/decarbonation/desulfurization), vibrational property and crystallite morphology. Analyzing the photoluminescence of Eu^{3+} and Sm^{3+} in the $Gd_2O_2SO_4$ typical host found that the 617 nm (Eu^{3+}, λ_{ex} = 275 nm) and 608 nm (Sm^{3+}, λ_{ex} = 407 nm) main emissions can retain as high as ~79.6 and 85.5% of their room-temperature intensities at 423 K, with activation energies of ~0.19 and 0.21 eV for thermal quenching, respectively. Application also indicated that both the phosphors have the potential for optical temperature sensing via the fluorescence intensity ratio (FIR) technology, whose maximum relative sensitivity reached ~2.70% K^{-1} for Eu^{3+} and 1.73% K^{-1} for Sm^{3+} at 298 K.

***Keywords**:* Layered hydroxide; $RE_2O_2SO_4$; Luminescence; Optical temperature sensing

1. Introduction

Rare-earth oxysulfates ($RE_2O_2SO_4$) constitute an important family of inorganic compounds since they may show unusual low temperature magnetic properties (RE = Gd, Tb, Dy, Ho, Er, Tm),[1-3] serve as the catalyst for automotive emission-control with their large capacity of oxygen storage (RE = La, Pr, Nd, Sm),[4,5] and exhibit interesting luminescent properties once properly activated (RE = La, Gd, Y).[6-8] $RE_2O_2SO_4$ was initially proposed to be orthorhombic in structure,[9] but later investigation through neutron, electron and X-ray diffraction found that it actually belongs to the monoclinic system (Space group $C2/c$).[10,11] The family of compounds all have a layered crystal structure formed by alternative stacking of the $[RE_2O_2]^{2+}$ main layers and inter-layer $[SO_4]^{2-}$ along the *a*-axis, where two opposite O atoms of each $[SO_4]$ tetrahedron are coordinated with the RE in two adjacent $[RE_2O_2]^{2+}$ layers.[10,11]

Thermal decomposition of $RE_2(SO_4)_3{\cdot}nH_2O$ is the most common method to prepare $RE_2O_2SO_4$,[4,12] but is accompanied by the release of toxic SO_x gas and has difficulty in particle morphology control. To avoid these problems, the precursor conversion method has been adopted to synthesize $RE_2O_2SO_4$ of smaller particle sizes. For example, Machida et al.[5,13,14] prepared $RE_2O_2SO_4$ (RE = Pr, Y) powders of ~100 nm by calcining a dodecyl sulfate precursor in air at 600 °C, and Zhong et al.[15] obtained $RE_2O_2SO_4$ powders of ~1 μm (RE = La, Pr-Lu) via thermal decomposition at 700 °C in air of a polymer precursor precipitated from the $RE(NO_3)_3$-NaOH-$C_4H_6O_4S_2$ (dimercaptosuccinic acid) reaction system. Both the methods, however, appear to be difficult in phase-purity control of the final product. Layered rare-earth hydroxides (LREHs) draw a wide range of research interest during recent years because of their peculiar crystal structure, rich interlayer chemistry and abundant functionality of the RE

element, but are limited to the two categories of $RE_2(OH)_5A\cdot nH_2O$ (A: typical of Cl^- or NO_3^-) and $RE_2(OH)_4SO_4\cdot nH_2O$ (SO_4^{2-}-LREH).[16-20] Especially, the appearance of SO_4^{2-}-LREH (RE = La-Lu lanthanide or Y; n = 0 or 2) provided a unique opportunity for the green synthesis of $RE_2O_2SO_4$, since the compound would directly dehydrate to $RE_2O_2SO_4$ upon being properly heated ($RE_2(OH)_4SO_4\cdot nH_2O \rightarrow RE_2O_2SO_4 + (n + 2)H_2O$).[18,19] The hydrated form of SO_4^{2-}-LREH ($RE_2(OH)_4SO_4\cdot 2H_2O$) can be synthesized for the relatively larger RE^{3+} (RE = La-Dy) via fluxing a mixed solution of RE sulfate, sodium sulfate (Na_2SO_4, mineralizer) and hexamethylenetetramine ($(CH_2)_6N_4$, precipitant) or via hydrothermal reaction of a mixed solution of RE nitrate and ammonium sulfate ($(NH_4)_2SO_4$) under ~100 °C and pH ~7-9.[17,19,20] The anhydrous form of SO_4^{2-}-LREH ($RE_2(OH)_4SO_4$) is obtainable for the relatively smaller RE^{3+} (RE = Eu-Lu and Y) via hydrothermal reaction under a strictly controlled temperature and solution pH, for example 150 °C and pH = 10 for RE = Eu and Gd, 150 °C and pH = 8-9 for RE = Tb and Dy, 150 °C and pH = 7 for RE=Ho, Er and Y, 180 °C and pH = 7 for RE = Er, Tm and Y, and 200 °C and pH = 7 for RE=Lu,[18] where the tending to be lower pH with decreasing radius of RE^{3+} was believed to be a reflection of lanthanide contraction. It is noteworthy that a certain amount of CO_3^{2-}, arising from atmospheric CO_2 or the hydrolysis of $(CH_2)_6N_4$ ($(CH_2)_6N_4 + H_2O \rightarrow CH_2O + NH_3$, $CH_2O + H_2O \rightarrow CO_2 + H_2$)[21] is readily incorporated into the $RE_2(OH)_4SO_4\cdot nH_2O$ formula, and the CO_3^{2-} was proposed to replace hydroxyls (OH^-) owing to its high coordinating capability.[17,22,23] However, it remains unclear that to what extent can the OH^- be replaced and how would CO_3^{2-} substitution affect crystal structure. To answer these questions, we autoclaved an aqueous solution of $Gd(NO)_3$, $(NH_4)_2SO_4$ and urea ($CO(NH_2)_2$) at 140 °C for 12 h, and obtained a precipitate that was

analyzed by a number of techniques to be $Gd_2(OH)_2CO_3SO_4{\cdot}nH_2O$ (n~1.5).[24] Structure analysis by applying multiple algorithms (ITO, DICVOL and TREOR) and Pawley refinement further revealed that the compound was crystallized in the tetragonal system (space group: P-42_1m) and is layer structured along the [001] crystallographic direction.[24] It was also found that calcining the compound in air at 800 °C may yield $Gd_2O_2SO_4$ via dehydration, dehydroxylation and decarbonation.[24] It still remains unclear, however, whether such a formula exists for the other RE elements and, if yes, how would lanthanide contraction (RE^{3+} size) affect the crystal structure and physicochemical properties of such a compound.

We thus performed hydrothermal synthesis for the full range of RE elements (RE = La-Lu lanthanides and Y) via reacting $RE(NO)_3$, $(NH_4)_2SO_4$ and Na_2CO_3 in this work, where Na_2CO_3 was employed as the CO_3^{2-} source instead of urea for an easier control of solution pH and CO_3^{2-} concentration, and such an initiation successfully produced $RE_2(OH)_2CO_3SO_4{\cdot}nH_2O$ (REOCSH) for RE = Gd-Lu and Y. The compounds were characterized in detail by a number of techniques to manifest the intrinsic influence of lanthanide contraction on crystal structure, thermal behavior, vibrational property and crystallite morphology. Calcining the REOCSH in air at 800 °C also produced the corresponding $RE_2O_2SO_4$ compound in each case, and the dependence of lattice parameters on RE^{3+} size was revealed. Through analysis of temperature-dependent photoluminescence, Eu^{3+} and Sm^{3+} doped $Gd_2O_2SO_4$ phosphors were demonstrated to possess satisfactory thermal stability and have the potential for optical thermometry via the fluorescence intensity ratio (FIR) technology.

2. Experimental Section

2.1. Reagents and hydrothermal synthesis

99.99% pure $Ce(NO_3)_3 \cdot 6H_2O$, Pr_6O_{11}, Tb_4O_7 and RE_2O_3 were purchased from Huizhou Ruier Rare-Chem. Hi-Tech. Co. Ltd (Huizhou, China), and analytical grade $(NH_4)_2SO_4$, Na_2CO_3, HNO_3 and NH_4OH were purchased from Sinopharm Co., Ltd (Shanghai, China). The rare-earth oxides listed above were separately dissolved with a proper amount of HNO_3 solution. Ultra-pure water (resistivity > 18 MΩ·cm) was used throughout the experiments.

In a typical synthesis of $RE_2(OH)_2CO_3SO_4 \cdot nH_2O$ (REOCSH), 1.5 mmol of $(NH_4)_2SO_4$ and 1.5 mmol of Na_2CO_3 were dissolved in 40 mL of water, to which 3 mmol of $RE(NO_3)_3$ was added under magnetic stirring, followed by pH adjustment with HNO_3 and NH_4OH while keeping the total volume at 60 mL. After 30 min of continuous stirring for homogenization, the mixture was transferred into a Teflon lined stainless steel autoclave of 100 mL capacity, followed by 24 h of reaction in an electric oven preheated at 140 °C. After natural cooling to room temperature, the precipitate was collected via centrifugation, washed with water and ethanol successively, and then dried at 60 °C for 12 h. With RE = Gd for example, a series of experiments were carried out to investigate the influence of solution pH. The Eu^{3+} and Sm^{3+} doped samples of $(Gd_{0.95}Eu_{0.05})_2(OH)_2CO_3SO_4 \cdot nH_2O$ and $(Gd_{1-x}Sm_x)_2(OH)_2CO_3SO_4 \cdot nH_2O$ (x = 0.005-0.03) were also synthesized according to the above procedure, where the content of Eu^{3+} was taken as the optimal value of 5 at.% according to a previous report on $La_2O_2SO_4:Eu^{3+}$.[25] Since the luminescence property of $Gd_2O_2SO_4:Sm^{3+}$ has not been reported before to the best of our knowledge, the Sm^{3+} content was varied to determine the optimal value. $RE_2O_2SO_4$ was produced by calcining the corresponding REOCSH in stagnant air at 800 °C for 1 h, using a heating rate of 8 °C/min for the ramp stage of heating.

2.2. Characterization

Phase identification was performed via X-ray diffractometry (XRD, SmartLab, Rigaku, Tokyo, Japan) under 40 kV/200 mA, using nickel-filtered Cu-Kα radiation (λ= 0.15406 nm) and a scanning speed of 4° 2θ/min. Product morphology and structure were analyzed by field emission scanning electron microscopy (FE-SEM, Model JSM-7001F, JEOL, Tokyo) under an acceleration voltage of 15 kV, transmission electron microscopy (TEM, Model JEM-2000FX, JEOL) under 200 kV, and atomic force microscopy (AFM, Model Nanosurf easyScan-2, Liestal, Switzerland) in the tapping mode with a scanning resolution of 256 points/line and a scanning rate of 1 s/line. Fourier transform infrared spectroscopy (FTIR, Nicolet iS5, Thermo Fisher Scientific, Waltham, USA) was conducted using the standard KBr pellet method. The elemental contents of the typical hydrothermal products were determined for RE via inductively coupled plasma-optical emission spectrometry (ICP-OES; Model iCAP 7400, Thermo Fisher Scientific) and for C and S via the inert gas fusion-infrared absorption/thermal conductivity technique (Elementar varioEL cube, Langenselbold, Germany). Thermogravimetry/differential thermal analysis (TG/DTA, Model SETSYS Evolution-16, Setaram, France) was performed at a constant heating rate of 10 °C/min in flowing simulated air (50 mL/min). Photoluminescence and fluorescence decay were analyzed with a Model FP-8600 fluorospectrophotometer (JASCO, Tokyo), using a 150 W xenon lamp for excitation, a scan speed of 100 nm/min, a slit width of 5 nm, and an HPC-836 accessory (JASCO) for temperature control.

3. Results and discussion

3.1 Characterization of the hydrothermal products

The $Gd_2(OH)_2CO_3SO_4{\cdot}nH_2O$ (GdOCSH) obtained from the $Gd(NO)_3$-$(NH_4)_2SO_4$-urea hydrothermal system in our previous work[24] is the only known $RE_2(OH)_2CO_3SO_4{\cdot}nH_2O$ (REOCSH) compound. The GdOCSH can be viewed as a derivative of $Gd_2(OH)_4SO_4{\cdot}nH_2O$ (SO_4^{2-}-LREH) since it can be yielded by replacing two out of four hydroxyls of the latter with CO_3^{2-}. The GdOCSH compound was analyzed to belong to the tetragonal system (space group: P-42_1m) with a crystal structure layered along the c-axis,[24] whose XRD pattern is shown in Fig. S1. Though the exact coordination of Gd yet needs to clarify, it was tentatively proposed by considering the layered structure of SO_4^{2-}-LREH[18,20] that the main layers (hydroxide layers) of GdOCSH would be composed of Gd^{3+}, OH^- and H_2O while the SO_4^{2-} and CO_3^{2-} anions are sandwiched between two adjacent hydroxide layers for charge balance. As aforesaid, urea ($CO(NH_2)_2$) does not allow a facile control of solution pH, though pH value may profoundly affect chemical potential and cation hydrolysis.[26-28] The influence of solution pH on hydrothermal product was thus examined in this work for the $Gd(NO)_3$-$(NH_4)_2SO_4$-Na_2CO_3 reaction system. It is seen from Fig. S2 that the pH = 6 and 7 products conform to GdOCSH,[24] though the pH = 6 one was much better crystallized, while the pH = 8 and 10 samples are essentially amorphous. Calcining the pH =10 product at 800 °C in air produced a phase mixture of cubic Gd_2O_3 (JCPDS No. 12-0797) and monoclinic $Gd_2O_2SO_4$ (JCPDS No. 24-9775),[8,18] as shown in Fig. S3a, indicating that the precipitate has an off-stoichiometric amount of SO_4^{2-} when compared with GdOCSH. In the current reaction system, Gd^{3+} would undergo hydration and hydrolysis to form $[Gd(OH)_a(CO_3)_b(SO_4)_c(H_2O)_d]^{3-a-2b-2c}$ complex ion,[26,27] in which SO_4^{2-} is less coordinating than CO_3^{2-}.[27] For this, a higher solution pH would increase the OH^-/Gd^{3+} and meanwhile

decrease the SO_4^{2-}/Gd^{3+} molar ratio of the complex ion to yield a precipitate that has less SO_4^{2-}.

As the above results imply that an alkaline environment is not conducive to GdOCSH formation, the synthesis of REOCSH was thus attempted under pH = 6 for the other RE elements. XRD analysis indicated that the La and Ce products are a mixture of hydroxyl carbonate ($RE(OH)CO_3$) and an unknown phase in each case, the Pr and Nd products are a mixture of $RE(OH)CO_3$ and $NaRE(SO_4)_2{\cdot}2H_2O$, the Sm and Eu products are amorphous (Fig. S4), and REOCSH is only obtainable for RE = Gd-Lu and Y (Fig. 1a). Noteworthy is that the Sm and Eu products yielded a mixture of RE_2O_3 and $RE_2O_2SO_4$ by calcination at 800 °C (Fig. S3b,c), indicating that they contain less SO_4^{2-} than the REOCSH formula. For composition verification of the claimed REOCSH, chemical analysis was performed for the four representative samples of RE = Gd, Ho, Lu and Y. From the results tabulated in Table S1 and by considering molecular neutrality, it can be concluded that the samples would indeed have the general formula of $RE_2(OH)_2CO_3SO_4{\cdot}nH_2O$, since in each case the RE:C:S atomic ratio is very close to 2:1:1. It should be noted that, through affecting RE^{3+} hydrolysis and the composition of $[RE(OH)_a(CO_3)_b(SO_4)_c(H_2O)_d]^{3-a-2b-2c}$ complex ion, reaction temperature and solution pH jointly affect REOCSH formation, as found by previous studies on the hydrothermal crystallization of SO_4^{2-}-LREH compounds.[18,19] Our preliminary experiments also showed that hydrothermal temperatures below 140 °C and above 180 °C would produce low-crystallinity REOCSH/amorphous mass and a mixture of REOCSH and impurity phase, respectively, and 140 °C and pH = 6 are the optimal parameters to obtain REOCSH of satisfactory crystallinity for an as wide as possible range of RE elements.

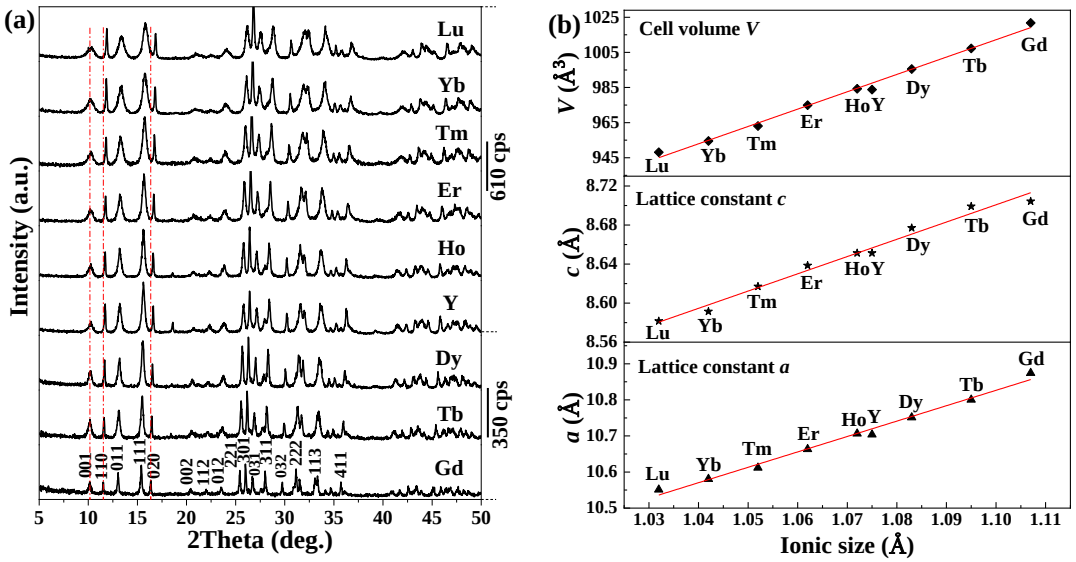

Fig. 1. XRD patterns (a) and correlation of lattice constants (a = b, c) and cell volume (V) with the ionic radius of RE^{3+} (b) for $RE_2(OH)_2CO_3SO_4{\cdot}nH_2O$.

Analyzing the XRD patterns of the series of REOCSH (Fig. 1a) with the Jade 6 software revealed that the cell parameters (a = b, c) and cell volume (V) almost linearly decrease with decreasing RE^{3+} size (Fig. 1b, coordination number CN = 9), conforming to lanthanide contraction. Nevertheless, the a parameter decreases much faster than c does, as perceived from the slopes of the corresponding plots (~4.27 for a and 1.77 for c). Such a phenomenon is mainly attributed to the layered crystal structure of REOCSH, and can be explained by considering that (1) the RE^{3+} ions are accommodated in the hydroxide main layers (ab planes), which makes the a parameter (a = b) more susceptible to the size variation of RE^{3+}, and (2) the rigid pillaring of interlayer SO_4^{2-}/CO_3^{2-} makes the crystal structure less deformable along the c-axis, as in the case of SO_4^{2-}-LREH.[18] The tendency of a and c variations conform to the observation that the diffraction peaks arising from ab planes, such as (110) and (020), were substantially shifted to larger angles with decreasing RE^{3+} size while the (001) diffraction (perpendicular to the c-axis) was not appreciably affected (Fig. 1a). The above results also imply that the tetragonal unit cell of REOCSH would be non-uniformly deformed along with decreasing radius of RE^{3+}.

FTIR analysis was performed for the series of REOCSH products to examine the contained chemical species, and the results are shown in Fig. 2. It is seen that, as found previously,[24] the Gd product exhibited vibrations at ~3553 cm^{-1} for the stretching of OH^- (ν_1) and at ~3420/1645 cm^{-1} for the stretching (ν_1)/bending (ν_2) of H_2O.[29,30] CO_3^{2-} absorptions were found at ~842 cm^{-1} (ν_2, weak) and in the regions of ~1390-1590 cm^{-1} (ν_3, strong) and 670-808 cm^{-1} (ν_4, medium strong), while the characteristic vibrations of SO_4^{2-} are well identifiable at ~1010 cm^{-1} (ν_1, weak) and in the regions of ~1025-1270 cm^{-1} (ν_3 strong) and 583-645 cm^{-1} (ν_4, medium strong).[24,29] No other type of anion is detectable. The other samples have spectral profiles very similar to that of GdOCSH, but their CO_3^{2-} and SO_4^{2-} vibrations were gradually shifted to larger wavenumbers with decreasing RE^{3+} size, indicating a stronger interaction of both the types of ligands with the RE^{3+} center. Such a phenomenon might be understood by considering that the positively charged hydroxide main layers will have a higher charge density with decreasing *a*/*b* lattice parameters (Fig. 1b), which attract the negatively charged CO_3^{2-} and SO_4^{2-} anions for a stronger bonding.

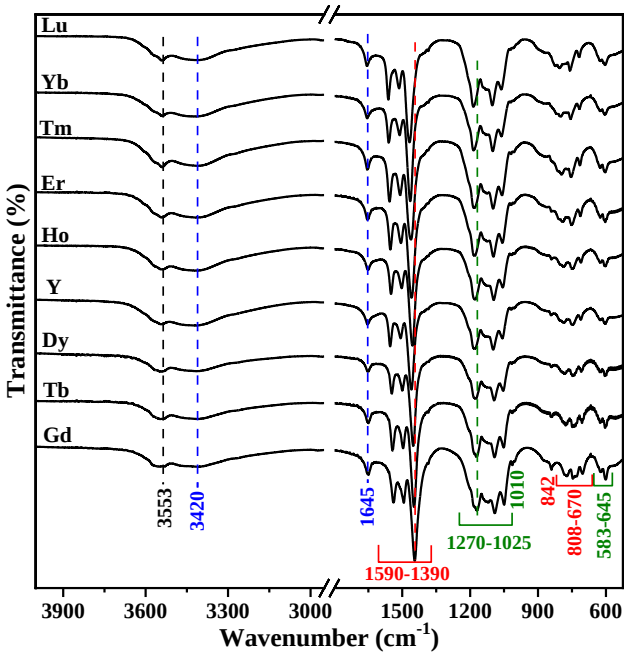

Fig. 2. FTIR spectra of the REOCSH products.

FE-SEM and TEM analysis found that the REOCSH compounds were all crystallized as nanoplates with edge lengths of up to ~400 nm, as shown in Fig. 3a-c for the typical samples of RE = Gd, Y and Lu and in Fig. S5 for the rest. It was noticed that the crystallites tend to be larger and less elongated as the RE^{3+} size decreases, which indicates a faster and more balanced development of the lateral dimensions (length and width). AFM analysis revealed that the thickness of the nanoplates tends to decrease with decreasing RE^{3+} size, which is ~20.9, 14.2 and 8.3 nm for RE = Gd, Y and Lu, respectively (Fig. 3d-f). The tending to be larger lateral dimension at a smaller RE^{3+} implies a lower density of REOCSH nucleation, which might be understood by considering that the stronger hydrolysis of RE^{3+} makes CO_3^{2-} and particularly SO_4^{2-} more difficult to reside in the coordination sphere of RE for the aforesaid $[RE(OH)_a(CO_3)_b(SO_4)_c(H_2O)_d]^{3-a-2b-2c}$ complex ion. For the same reason, the thickness development of REOCSH crystallites, which occurs via repetitive stacking of the hydroxide main layers and interlayer CO_3^{2-}/SO_4^{2-} along the [001] direction, was restricted to produce thinner nanoplates. Besides, the much smaller thickness than lateral dimension and the tending to be smaller thickness may explain why the 00*l* diffractions (such as 001) are significant broadened than the non-00*l* ones and why the (001) diffraction tends to be broader with decreasing RE^{3+} size (Fig. 1a), respectively. Selected area electron diffraction from an individual GdOCSH nanoplate yielded a set of well-arranged spots (SAED, the inset of Fig. 3a), among which those with the measured *d*-spacings of ~5.44/5.43 and 7.67 Å can be assigned to (010)/(100) and (110) planes, respectively. In addition, the (010)/(100) dihedral angle was found from the SAED pattern to be ~90°, well conforming to the tetragonal structure of GdOCSH.

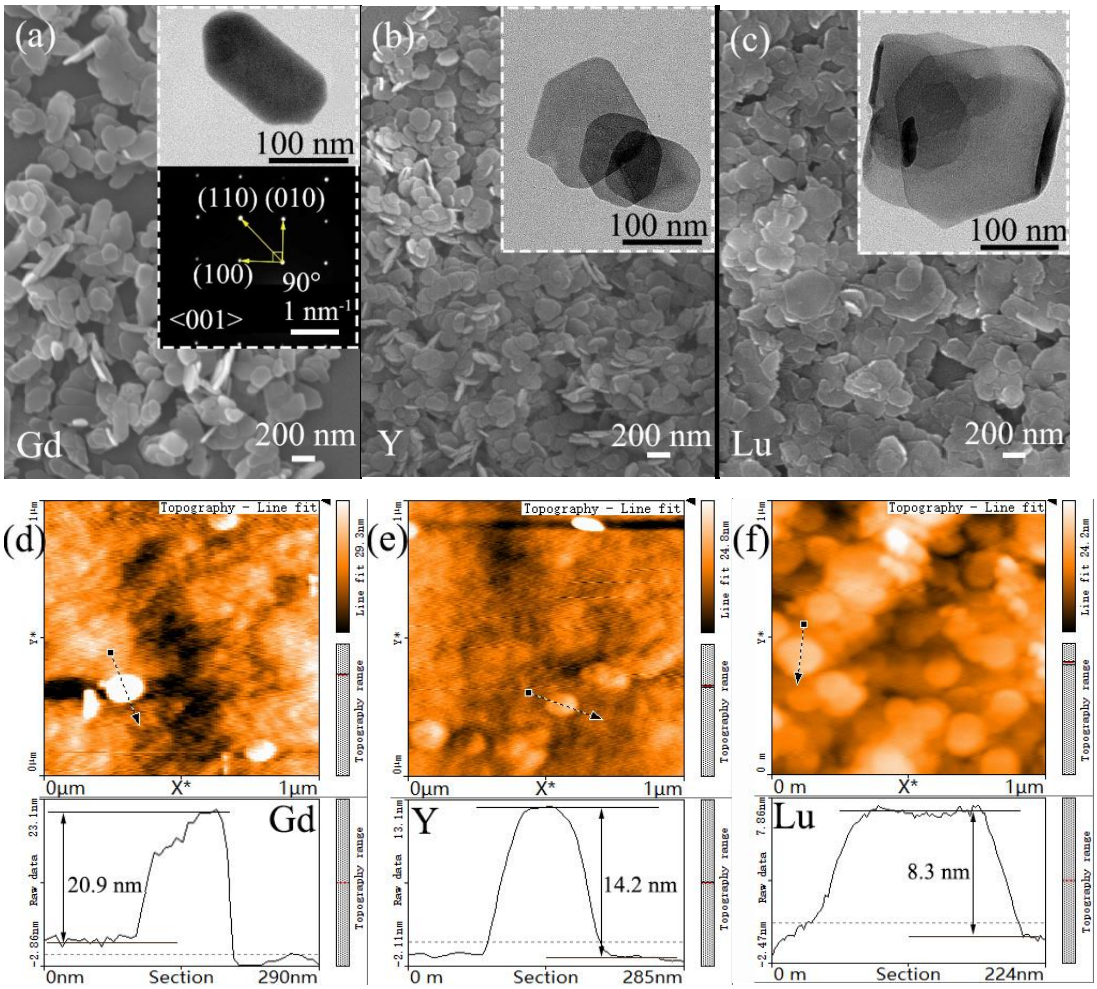

Fig. 3. FE-SEM/TEM (a-c) and AFM (d-f) analysis of the typical REOCSH products of RE = Gd, Y and Lu. In parts (d-f), the height profiles (lower row) were measured along the dashed black arrows in the AFM images (upper row) in each case.

The thermal behaviors of REOCSH were investigated by TG/DTA in flowing simulated air, and the results are shown in Fig. 4a for the TmOCSH representative and in Fig. S6 for the rest. It is seen that the compounds similarly decompose via five stages corresponding to dehydration (stage I), partial dehydroxylation (stage II), complete dehydroxylation/partial decarbonation (stage III), complete decarbonation (stage IV), and desulfurization (stage V).[24] Unlike the other stages, stage IV is companioned by an exotherm in each case, which corresponds to the crystallization of $RE_2O_2SO_4$. The decomposition data are tabulated in Table 1 for the entire series of REOCSH, together with the number of molecular water (*n* value) calculated from the first stage of decomposition. The good correspondence of the

observed (Table 1) and theoretical (Table S2) weight losses may further confirm the proposed decomposition procedures. The dehydroxylation, decarbonation and desulfurization of RE compounds would shift to a higher, lower and lower temperature with decreasing RE^{3+} size, respectively,[19,31,32] and the phenomena can be explained from the Pearson hard-soft-acid-base (HSAB) theory by considering lanthanide contraction. As seen from the peak temperature of the thermal event (Table 1), the stage III and stage V of this work follow the aforesaid tendency but stage IV showed an opposite trend. It was speculated that the gradually higher occurrence temperature of stage IV (complete decarbonation) is owing to more sluggish removal of hydroxyls.

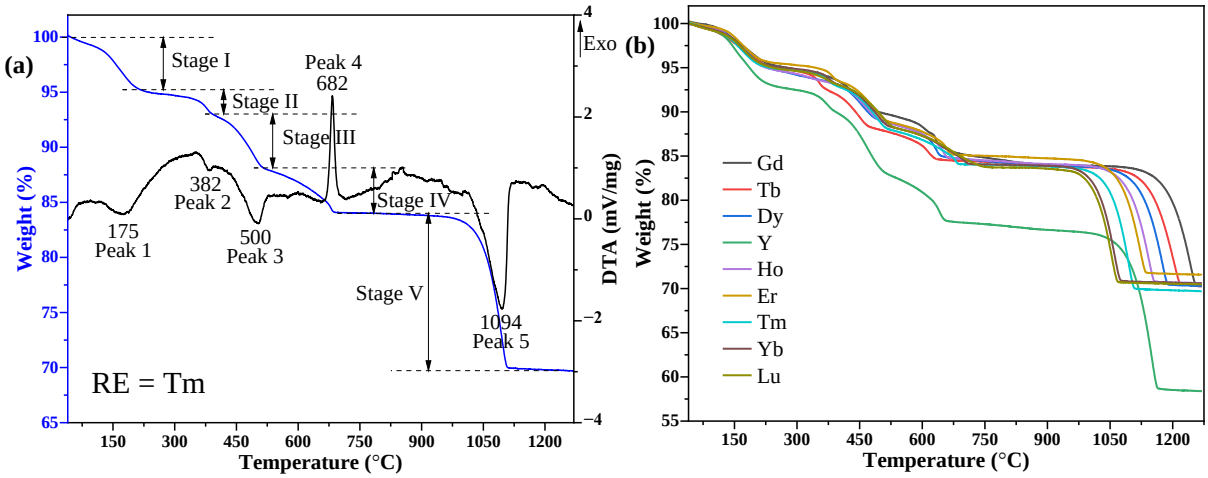

Fig. 4. TG/DTA curves for TmOCSH (a) and a comparison of the TG curves for the full series of REOCSH compounds (b).

Table 1 A summary of the thermal decomposition data for the series of REOCSH compounds

RE	Peak 3 (°C)	Peak 4 (°C)	Peak 5 (°C)	*n* value	Weight loss I (%)	Weight loss II-IV (%)	Weight loss V (%)	Total weight loss (%)
Gd	457	614	1246	1.44	4.88	11.00	14.54	30.42
Tb	459	616	1211	1.43	4.81	10.83	14.60	30.24
Dy	467	630	1173	1.47	4.89	10.83	13.91	29.76
Y	487	645	1151	1.53	6.97	15.40	19.33	41.70
Ho	478	651	1143	1.53	5.03	10.45	13.93	29.41
Er	500	660	1124	1.31	4.31	10.48	13.61	28.40
Tm	500	682	1094	1.46	4.74	11.22	14.28	30.24
Yb	504	707	1063	1.47	4.69	10.96	13.85	29.50
Lu	515	750	1057	1.57	4.97	10.81	13.79	29.57

3.2 Derivation and characterization of $RE_2O_2SO_4$

According to the results of TG (Fig. 4b), 800 °C was selected as a suitable temperature to derive $RE_2O_2SO_4$ from REOCSH. XRD analysis (Fig. 5a) showed that phase-pure $RE_2O_2SO_4$ (monoclinic, space group $C2/c$)[8,18] was obtained in each case, but the diffraction peaks gradually shifted to higher angles with decreasing size of RE^{3+}. Analyzing the XRD patterns with the Jade 6 software found that lattice constants (a, b and c) and cell volume (V) tend to linearly decrease as the radius of RE^{3+} decreases while axis angle β showed an opposite tendency (Fig. 5b, Table S3). FE-SEM observation indicated that the nanoplates of REOSCH tend to disintegrate by the mass loss during calcination and the primary crystallites of $RE_2O_2SO_4$ are up to ~25 nm (Fig. S7). This size value is in line with the average crystallite sizes (~22 nm, Table S3) estimated by broadening analysis of the XRD peaks (Fig. 5a) with Scherrer formula.

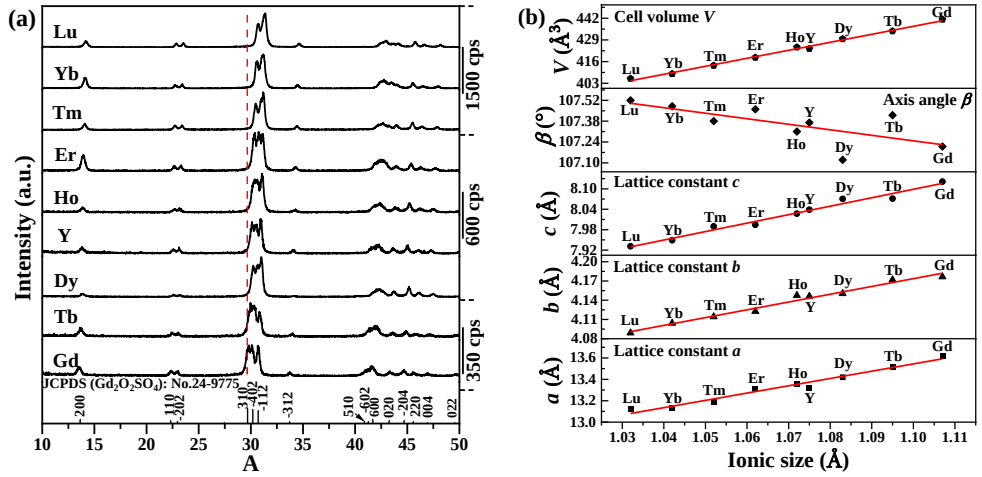

Fig. 5. XRD patterns of the derived $RE_2O_2SO_4$ (a) and correlation of lattice parameters (a, b, c, β) and cell volume (V) with the ionic radius of RE^{3+} (b).

The above results thus indicated that the incorporation of a pretty high amount of CO_3^{2-} into SO_4^{2-}-LREH to form $RE_2(OH)_{4-2x}(CO_3)_xSO_4{\cdot}nH_2O$ ($x \leq 1.0$) would not cause phase separation (formation of RE_2O_3) by calcination at 800 °C for RE = Gd-Lu lanthanide or Y. It can also be inferred that property control of $RE_2O_2SO_4$ powder is viable through precursor engineering

and that precursor synthesis can be performed under much less stringent conditions (such as lower temperatures in open air), since as long as the precursor has the above formula, no matter it is crystalline or amorphous, $RE_2O_2SO_4$ can be derived from it by proper annealing.

3.3 The photoluminescence properties of $Gd_2O_2SO_4$:0.05Eu^{3+} and $Gd_2O_2SO_4$:xSm^{3+}

The Eu^{3+} and Sm^{3+}-doped samples of $(Gd_{0.95}Eu_{0.05})_2(OH)_2CO_3SO_4 \cdot nH_2O$ (GdOCSH:0.05Eu) and $(Gd_{1-x}Sm_x)_2(OH)_2CO_3SO_4 \cdot nH_2O$ (x = 0.005-0.03; GdOCSH:xSm) were synthesized under the same hydrothermal conditions of GdOCSH. Phase analysis indicated that the products conform to GdOCSH and do not contain any impurity (Fig. S8a). Elemental mapping of the GdOCSH:0.05Eu and GdOCSH:0.03Sm typical samples revealed that the constituent elements are uniformly distributed across the crystallites (Fig. 6), implying the formation of solid solution. XRD analysis showed that phase-pure $Gd_2O_2SO_4$:0.05Eu and $Gd_2O_2SO_4$:xSm were produced by calcining their respective precursors in air at 800 °C (Fig. S8b). The formation of GdOCSH:Ln^{3+} and $Gd_2O_2SO_4$:Ln^{3+} (Ln = Eu, Sm) solid solutions were further evidenced by lattice expansion (Table S4), since the effective ionic radii of Eu^{3+} (1.12 Å, CN = 9) and Sm^{3+} (1.132 Å, CN = 9) are both larger than that of Gd^{3+} (1.107 Å, CN = 9).[33]

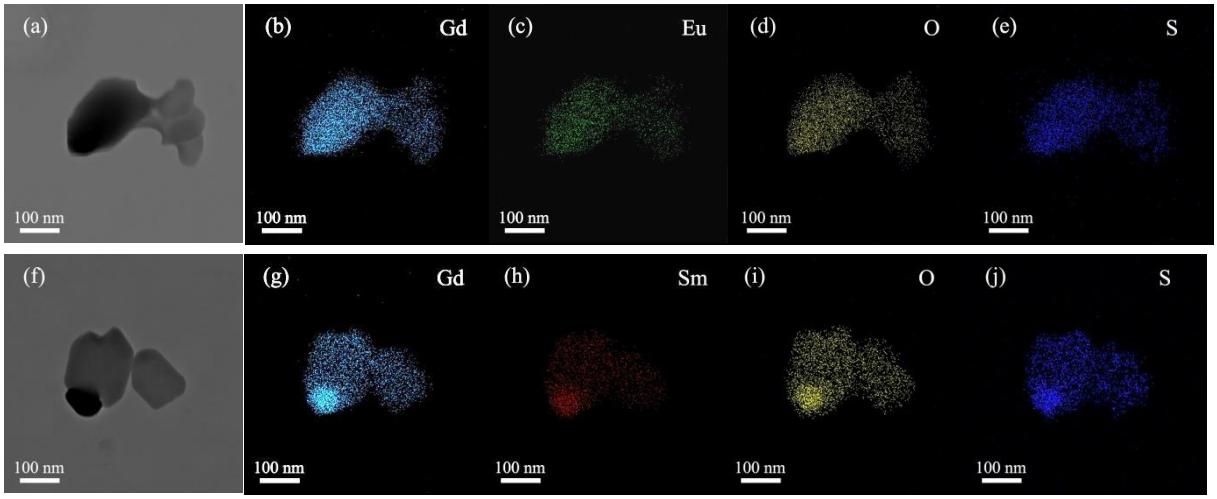

Fig. 6. STEM morphologies (a, f) and the results of elemental mapping for GdOCSH:0.05Eu (a-e) and GdOCSH:0.03Sm (f-j).

Fig. 7a shows the excitation (PLE) and emission (PL) spectra of $Gd_2O_2SO_4$:0.05Eu. It is seen that the PLE spectrum, taken by monitoring the 617 nm red emission, contains a broad and strong band centered at ~275 nm for $O^{2-} \rightarrow Eu^{3+}$ charge transfer and $^8S_{7/2} \rightarrow {}^6L_J$ transition of Gd^{3+} and a few much weaker peaks in the longer wavelength region for intra-4f^6 transitions of Eu^{3+}.[34,35] Under 275 nm excitation, the phosphor exhibited the typical $^5D_0 \rightarrow {}^7F_J$ (J = 0-4) emissions of Eu^{3+}, with the $^5D_0 \rightarrow {}^7F_2$ one (~617 nm) being the most prominent. The phosphor has a quantum yield (QY) of ~32.3% and Commission Internationale de L'Eclairage (CIE) chromaticity coordinates (Fig. S9) of around (0.656, 0.344). It was also found that the 617 nm main emission decayed in a single exponential manner and has a fluorescence lifetime of ~2.43 ± 0.01 ms (Fig. 7c).

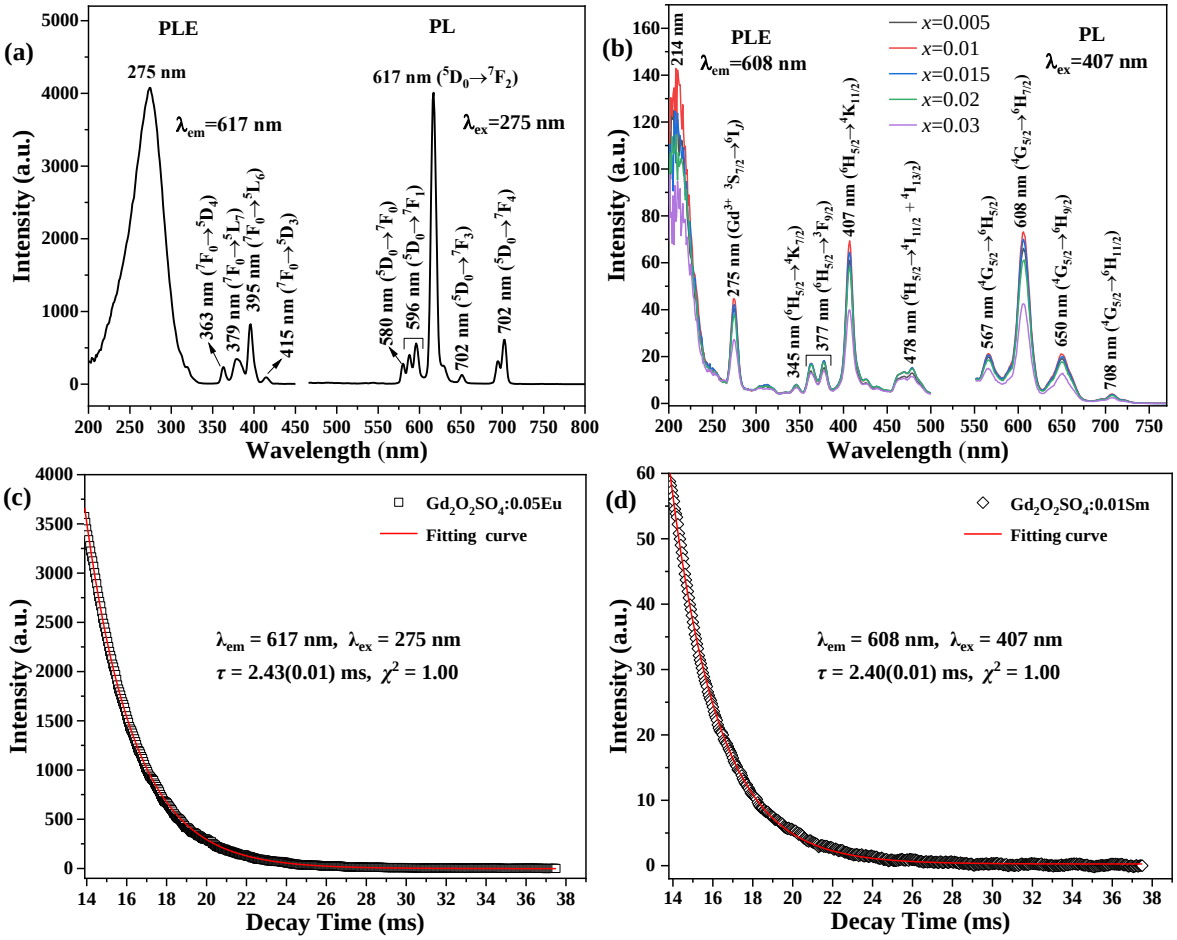

Fig. 7. PLE and PL spectra (a, b) and fluorescence decay curves (c, d) of $Gd_2O_2SO_4$:0.05Eu (a, c) and $Gd_2O_2SO_4$:xSm (b, d) phosphors.

Fig. 7b shows the photoluminescence spectra of the series of $Gd_2O_2SO_4$:*x*Sm phosphors. It is seen that the PLE spectra, recorded by monitoring the 608 nm main emission, consist of three parts in each case, with the peaks centered at ~214 and 275 nm for $O^{2-} \rightarrow Sm^{3+}$ charge transfer and $^8S_{7/2} \rightarrow {}^6I_J$ transition of Gd^{3+}, respectively,[36,37] and the ones in the 325-500 nm region for intra-$4f^5$ transitions of Sm^{3+}. Since 214 nm is too close to the vacuum ultraviolet region, PL spectra were taken under 407 nm excitation ($^6H_{5/2} \rightarrow {}^4K_{11/2}$ transition, the second strongest). It is clear that the phosphors emit at 567, 608 (the strongest), 650 and 780 nm in each case, which can be assigned to transitions from the $^4G_{5/2}$ excited level to $^6H_{5/2}$, $^6H_{7/2}$, $^6H_{9/2}$ and $^6H_{11/2}$ ground states of Sm^{3+}, respectively. The intensity of emission improves with increasing Sm^{3+} concentration up to x = 0.01, followed by a gradual decrease owing to concentration quenching. The operating mechanism of concentration quenching can be analyzed with the following equation:[38]

$$\log\left(\frac{I}{x}\right) = \left(-\frac{s}{3}\right)\log(x) + a \quad (1)$$

where I is the intensity of the 608 nm emission, x is the content of Sm^{3+}, a is a constant, and s is an indicator of interaction type, with the values of 3, 6, 8, and 10 for exchange, electric dipole-dipole, electric dipole-quadrupole, and electric quadrupole-quadrupole interactions, respectively. Linear fitting of the log(I/x) versus log(x) plot yielded an s value of ~4.50 (Fig. S10), which is midway between 3 and 6. To differentiate exchange interaction from electric dipole-dipole interaction, we analyzed the separation distance (R) of Sm^{3+} with the equation $R \approx 2[3V/(4\pi xN)]^{1/3}$,[39] where V is the volume of the unit cell (~441.3 Å^3) and N is the number of Gd^{3+} sites in the unit cell (N = 8), and found R values of ~2.19, 1.92, 1.74 and 1.52 nm for x = 0.01, 0.015, 0.02 and 0.03, respectively. As the R values are all obviously larger than the ~0.4

nm required for exchange interaction, it can be said that concentration quenching largely took place via electric dipole-dipole interaction for $Gd_2O_2SO_4$:*x*Sm. The $Gd_2O_2SO_4$:0.01Sm optimal composition was analyzed from its PL spectrum to have CIE color coordinates (Fig. S9) of about (0.593, 0.407) and QY of ~14.7%. Fluorescence decay analysis via single-exponential fitting found that the 608 nm main emission of $Gd_2O_2SO_4$:0.01Sm has a lifetime of ~2.40 ms (Fig. 7d).

3.4 Thermal stability and temperature sensing performance of $Gd_2O_2SO_4$:0.05Eu and $Gd_2O_2SO_4$:0.01Sm

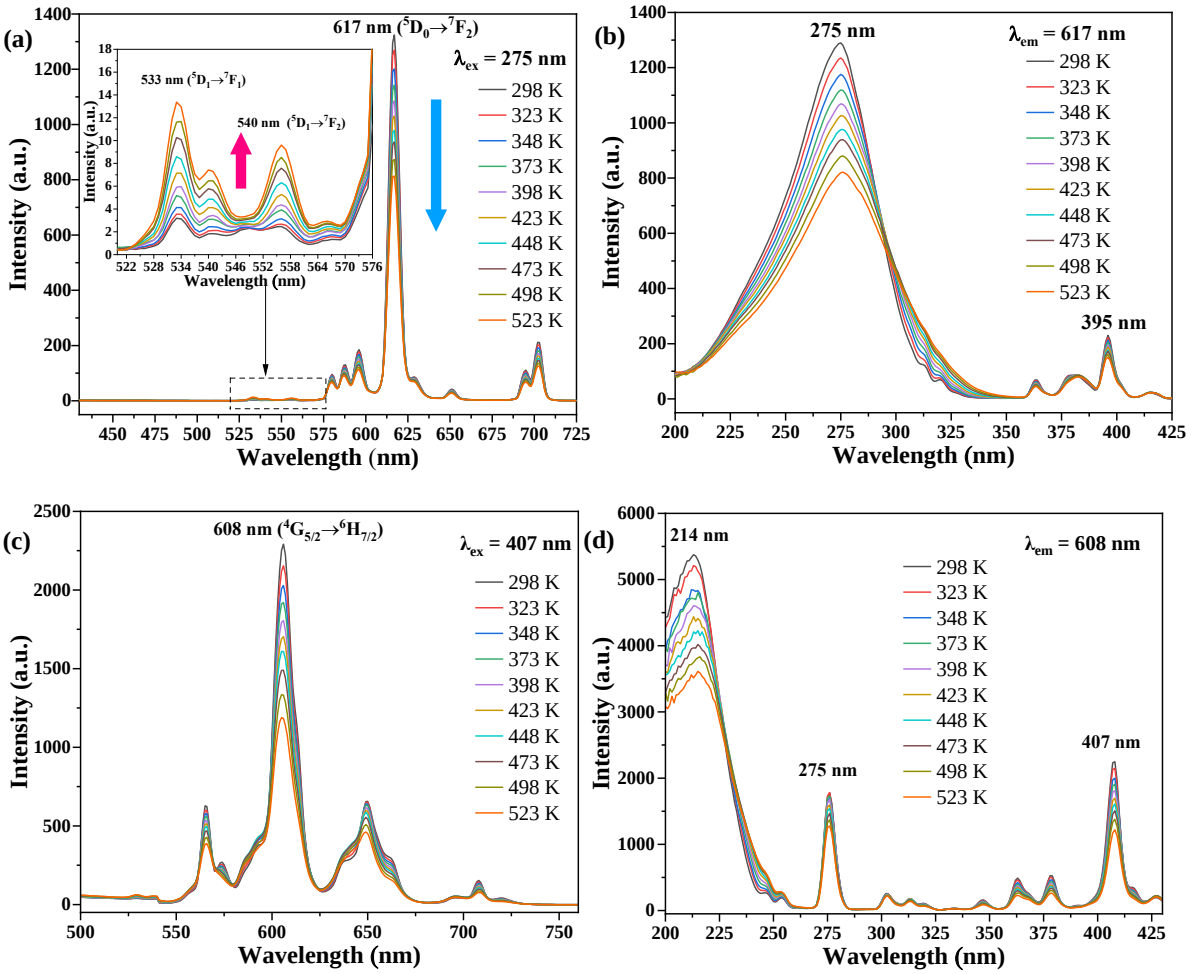

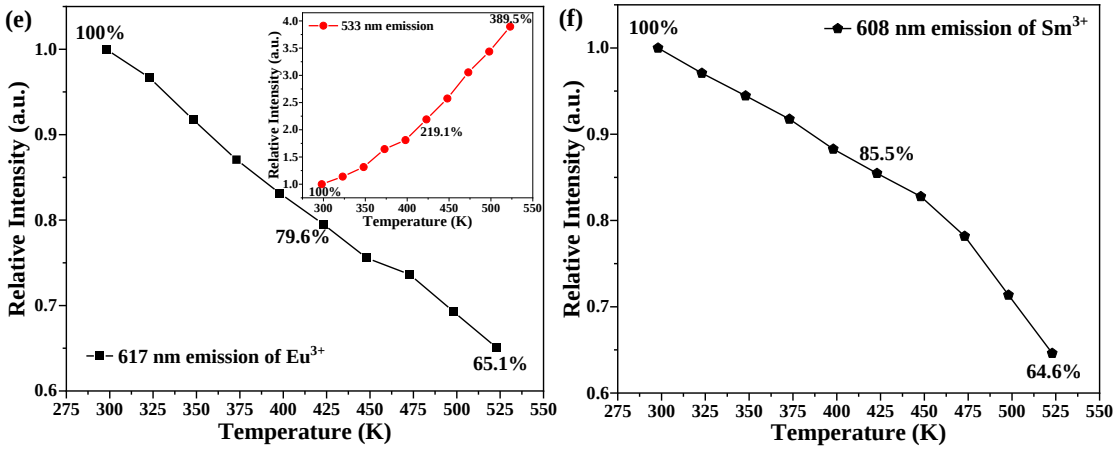

Fig. 8. Temperature-dependent emission (a, c) and excitation (b, d) spectra of the $Gd_2O_2SO_4$:0.05Eu (a, b) and $Gd_2O_2SO_4$:0.01Sm (c, d) phosphors. Parts (e) and (f) are for relative intensities of the 617 and 608 nm emissions of Eu^{3+} and Sm^{3+}, respectively. The insets in (a) and (e) respectively show an enlarged view of the 520-576 nm region and relative intensity of the 533 nm emission of Eu^{3+}.

To examine thermal stability, temperature-dependent photoluminescence spectra (298-523 K) were taken in Fig. 8 for the $Gd_2O_2SO_4$:0.05Eu and $Gd_2O_2SO_4$:0.01Sm phosphors. It is seen that the $^5D_0 \rightarrow {}^7F_J$ (J = 0–4) emissions of $Gd_2O_2SO_4$:0.05Eu (Fig. 8a) and the $^4G_{5/2} \rightarrow {}^6H_{P/2}$ (P = 5, 7, 9, 11) emissions of $Gd_2O_2SO_4$:0.01Sm (Fig. 8c) were gradually weakened with increasing temperature owing to thermal quenching, though appreciable change in peak shape/position was not found. Noteworthy is that the $^5D_1 \rightarrow {}^7F_{1,2}$ luminescence of Eu^{3+} was steadily enhanced by a higher temperature, as revealed by an enlarged view of the 520-576 nm spectral region (the inset in Fig. 8a) and temperature-dependent relative intensity of the 533 nm emission ($^5D_1 \rightarrow {}^7F_1$ transition, the inset in Fig. 8e). This is due to thermal coupling of the $^5D_0$ and $^5D_1$ energy levels, which makes $^5D_0$ electrons be readily promoted to the higher lying $^5D_1$ level by thermal activation. The $Gd_2O_2SO_4$:0.05Eu and $Gd_2O_2SO_4$:0.01Sm phosphors exhibited good thermal stability and their 617 nm ($^5D_0 \rightarrow {}^7F_2$) and 608 nm ($^4G_{5/2} \rightarrow {}^6H_{7/2}$) main emissions maintained ~79.6 and 85.5% of their room-temperature intensities at 423 K, respectively (Fig. 8e,f). The activation energy (E_a) of thermal quenching can be assayed with the Arrhenius equation:[40]

$$I_T = \frac{I_0}{1 + c\exp\left(-\frac{E_a}{kT}\right)} \quad (2)$$

where I_0 and I_T are the emission intensities at room temperature and temperature T, respectively, c is a rate constant, and k is the Boltzmann constant (8.629×10^{-5} eV/K). From the $\ln(I_0/I_T - 1)$ versus $1/(kT)$ plots shown in Fig. 9, E_a values of ~0.19 and 0.21 eV were derived via linear fitting for the 617 and 608 nm emissions of $Gd_2O_2SO_4$:0.05Eu and $Gd_2O_2SO_4$:0.01Sm, respectively.

From the temperature-dependent excitation spectra of $Gd_2O_2SO_4$:0.05Eu (Fig. 8b) and $Gd_2O_2SO_4$:0.01Sm (Fig. 8d), it was found that the intensity of each excitation peak also gradually decreases with increasing temperature by thermal quenching. Noteworthy is that temperature-induced red shift of charge transfer band (CTB) edge was clearly observed in both the cases, which is owing to increased population of higher vibrational sublevels of the ground state with increasing temperature.[41,42]

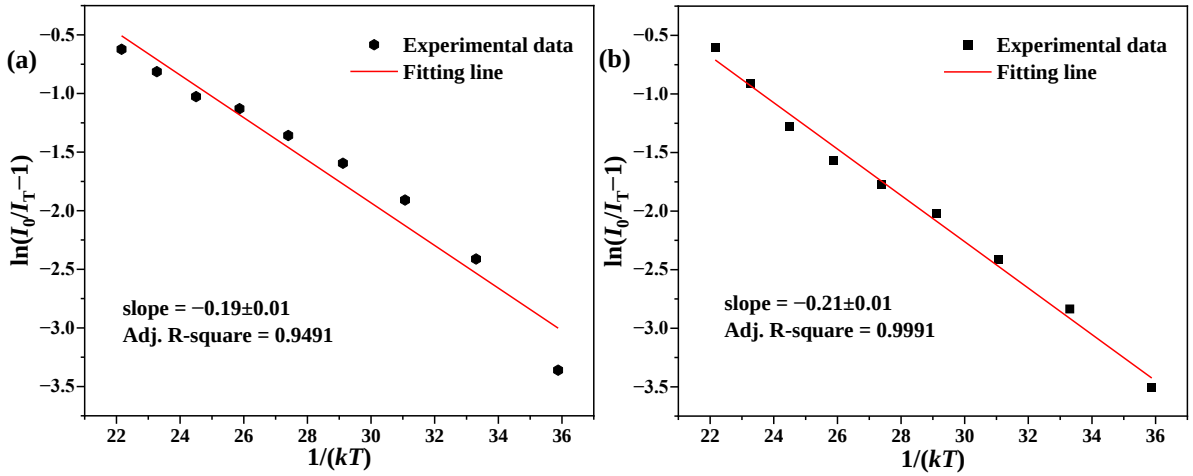

Fig. 9. $\ln(I_0/I_T - 1)$ vs. $1/(kT)$ plots for the 617 nm emission of $Gd_2O_2SO_4$:0.05Eu (a) and the 608 nm emission of $Gd_2O_2SO_4$:0.01Sm (b).

Non-contact temperature sensing with the fluorescence intensity ratio (FIR) technology is arousing a wide range of interest in recent years.[43] The FIR technology mostly utilizes the up-conversion luminescence of thermally coupled energy levels (TCLs), particularly the

$^4F_{7/2}/^4F_{3/2}$ of Nd^{3+}, the $^3F_{2,3}/^3H_4$ of Tm^{3+} and the $^2H_{11/2}/^4S_{3/2}$ of Er^{3+},[44] but the accuracy of temperature sensing is affected by the heating effect of the infrared excitation light. The problem can nevertheless be avoided by employing down-conversion luminescence. Especially, highly sensitive temperature sensing was recently achieved with the non-TCLs FIR technology, which utilized temperature-induced shift of CTB edge in vanadate systems doped by activators like Eu^{3+} and Sm^{3+}.[42,45]

For $Gd_2O_2SO_4$:0.05Eu, the FIR of the thermally coupled $^5D_1/^5D_0$ levels of Eu^{3+} can be described by the following offset-corrected Boltzmann equation:[43]

$$FIR(^5D_1/^5D_0) = \frac{I_1}{I_2} = A\exp\left(-\frac{\Delta E_f}{kT}\right) + B \quad (3)$$

where I_1 and I_2 represent the integral intensities of the $^5D_1 \rightarrow {}^7F_1$ (533 nm) and $^5D_0 \rightarrow {}^7F_2$ (617 nm) luminescence under 275 nm excitation, respectively, A is a fitting constant, ΔE_f is the energy gap between $^5D_0$ and $^5D_1$, k is the Boltzmann constant, T is the absolute temperature, and B is an offset factor. With the intensity data presented in Fig. 8e, it was found that $FIR(^5D_1/^5D_0)$ follows the equation $FIR(^5D_1/^5D_0) = 1.73\exp(-2396.02/T) + 0.003$ (Fig. 10a), and the derived ΔE_f value of 1667 cm^{-1} is in good agreement with that (1745 cm^{-1}) assayed from the emission spectra (Fig. 8a). The results thus indicate that the $^5D_1$ and $^5D_0$ levels of Eu^{3+} can be utilized for temperature sensing. On the other hand, the 617 nm emission of $Gd_2O_2SO_4$:0.05Eu under 325 nm excitation (CTB edge, Fig. 8b) and 395 nm excitation ($^5F_0 \rightarrow 5L_6$ transition, Fig. 7a) gradually gained and lost intensity with increasing temperature (Fig. S11) owing to red-shift of CTB edge and thermal quenching, respectively. These opposite tendencies provided an opportunity for thermal sensing, and analyzing the data shown in Fig. 10b found an equation of $FIR(I_{325}/I_{395}) = 85.02\exp(-2408.09/T) + 0.129$, where I_{325} and I_{395}

represent integral intensities of the 617 nm emission under 325 and 395 nm excitation, respectively. Opposite tendencies of temperature influence (Fig. 8f, Fig. S12) were also found for the 608 nm emission of $Gd_2O_2SO_4$:0.01Sm under excitation at 244 nm (CTB edge, Fig. 8d) and 407 nm ($^6H_{5/2} \rightarrow {}^4K_{11/2}$ transition, Fig. 7b). As shown in Fig. 10c, fluorescence intensity ratio $FIR(I_{244}/I_{407})$ follows the equation $FIR(I_{244}/I_{407}) = 10.06\exp(-1533.4/T) + 0.116$.

The performance of temperature measurement can be evaluated by absolute sensitivity (S_a) and relative sensitivity (S_r). It is well recognized that S_r is more practical than S_a,[46] and is more widely used to evaluate the performance of temperature sensing. S_r can be correlated to FIR and ΔE_f via the equation:[47]

$$S_r = \frac{1}{FIR}\frac{dFIR}{dT} = \frac{\Delta E_f}{kT^2} \quad (4)$$

For $Gd_2O_2SO_4$:0.05Eu, both the $S_r(^5D_1/^5D_0)$ and $S_r(I_{325}/I_{395})$ tend to decrease with increasing temperature, following the equations of $S_r(^5D_1/^5D_0) = 2396.02/T^2$ (Fig. 10d) and $S_r(I_{325}/I_{395}) = 1954.33/T^2$ (Fig. 10e), and have almost the same maximum value of ~2.70% K^{-1} at $T = 298$ K. The value is higher than those of most Eu^{3+}-activated thermosensitive materials, such as 1.4% K^{-1} at 300 K for $CaEu_2(WO_4)_4$,[48] 1.68% K^{-1} at 298 K for $GdVO_4$:0.12Eu,[49] 1.8% K^{-1} at 333 K for YBO_3:0.02Eu[50] and 2.23% K^{-1} at 298 K for $NaLaCaWO_6$:0.3Eu,[51] but is lower than the 4.36% K^{-1} at 300 K for YVO_4:0.1Eu.[52] The $S_r(I_{244}/I_{407})$ of $Gd_2O_2SO_4$:0.01Sm follows the equation $S_r(I_{244}/I_{407}) = 1533.40/T^2$ and has its maximum value of ~1.73% K^{-1} at 298 K (Fig. 10f), which is lower than the 3.68% K^{-1} at 300 K for $GdVO_4$:0.05Sm[42] and the 1.80% K^{-1} at 300 K for $GdNbTiO_6$:0.03Sm[53] but is larger than the 1.60% K^{-1} at 300 K for La_3NbO_7:0.01Sm.[54] It was also noticed that the maximum S_r values of both $Gd_2O_2SO_4$:0.05Eu and $Gd_2O_2SO_4$:0.01Sm are significantly larger than those of the recently reported

$Li_6CaLa_2Nb_2O_{12}$:Yb,Er (1.6% K^{-1} at 298 K),[55] $Sr_3Y(PO_4)_3$:Yb,Ho (1.1% K^{-1} at 298 K)[56] and $NaLuF_4$:Yb,Er (0.5% K^{-1} at 300 K)[57] up-conversion phosphors, though inferior to those of La_2MoO_6:Yb,Er (3.3% K^{-1} at 298 K)[58] and Bi_2MoO_6:0.02Er,0.02Tm,0.15Yb (5.90 % K^{-1} at 293 K).[59]

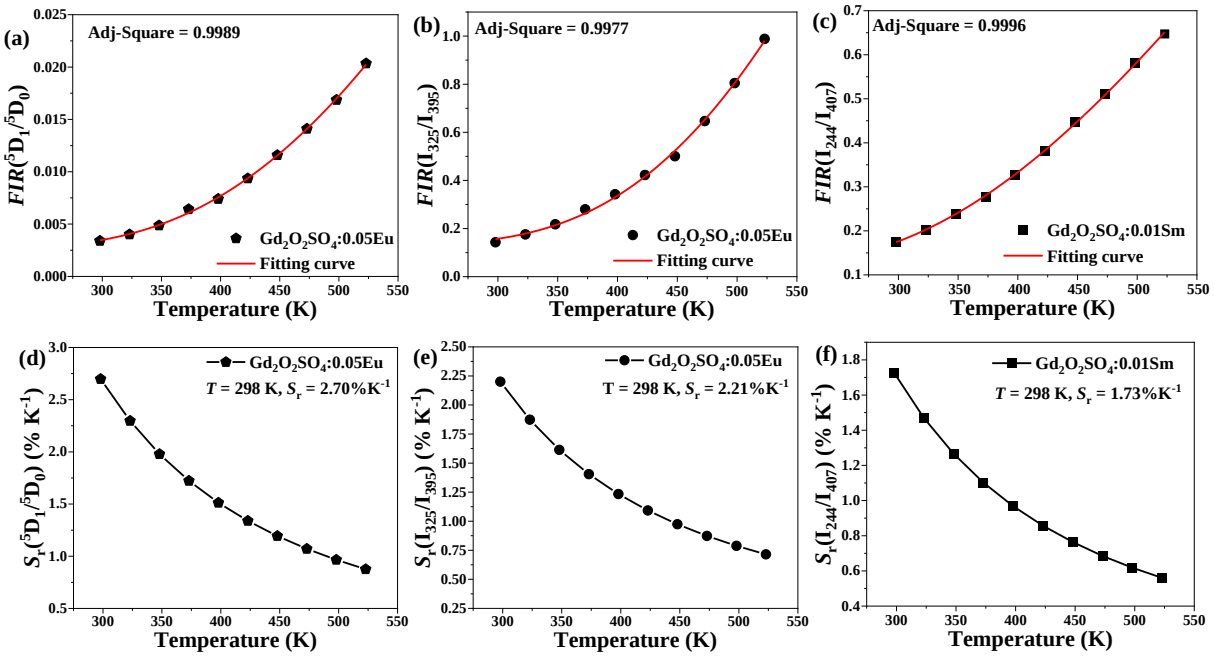

Fig. 10. *FIR* (a-c) and S_r (d-f) as a function of temperature for $Gd_2O_2SO_4$:0.05Eu and $Gd_2O_2SO_4$:0.01Sm.

Temperature resolution (δT) manifests the minimal detectable temperature change of a luminescent thermometer, which is defined as:[60,61]

$$\delta T = \frac{1}{S_r} \times \frac{\delta FIR}{FIR} \quad (5)$$

where $\delta FIR/FIR$ is the relative uncertainty of *FIR* and is dependent on the experimental setup. In our case, the $\delta FIR/FIR$ value was taken as 0.4% according to the standard deviation of the baseline reading fluctuation at 298 K. Therefore, the $\delta T(^5D_1/^5D_0)$ and $\delta T(I_{325}/I_{395})$ of $Gd_2O_2SO_4$:0.05Eu are ~0.15 and 0.18 K at 298 K, respectively, and the $\delta T(I_{244}/I_{407})$ of $Gd_2O_2SO_4$:0.01Sm is ~0.23 K at 298 K.

Repeatability and reversibility are important for practical application of a luminescent

thermometer. Three cycles of heating-cooling tests were conducted in this work for the two types of phosphors, and the results are shown in Fig. 11. It is seen that the *FIR*($^5D_1/^5D_0$) and *FIR*(I_{325}/I_{395}) of $Gd_2O_2SO_4$:0.05Eu (Fig. 11a,b) and the *FIR*(I_{244}/I_{407}) of $Gd_2O_2SO_4$:0.01Sm (Fig. 11c) are essentially fully reversible for each cycle and are quite stable at each temperature point for the three cycles. The average repeatability factor (R_c) was quantified with the following equation to be better than 98.7% for both the types of optical thermometers:[60]

$$R_c = 1 - \frac{\max|\Delta_c - \Delta_i|}{\Delta_c} \quad (6)$$

where Δ_i is the thermometric signal (*FIR*) at temperature *i* in each cycle and Δ_c is the mean of three Δ_i values. The results thus indicated that both the types of thermometers have good repeatability and reversibility for optical temperature sensing.

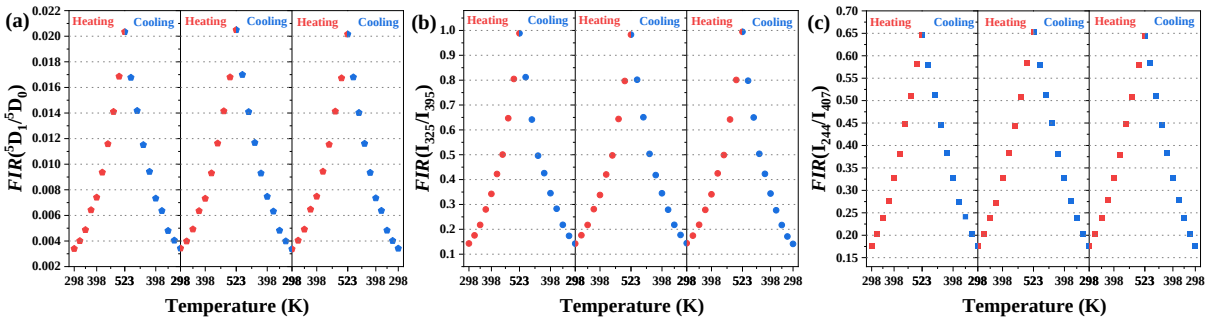

Fig. 11. Reversibility and repeatability tests of *FIR* for $Gd_2O_2SO_4$:0.05Eu (a, b) and $Gd_2O_2SO_4$:0.01Sm (c).

4. Conclusion

$RE_2(OH)_2CO_3SO_4 \cdot nH_2O$ was obtained in this work as a new type of layered hydroxide for RE = Gd-Lu lanthanides and Y. Non-uniform contraction of the unit cell, stronger interaction of CO_3^{2-}/SO_4^{2-} with the hydroxide main layers, increasing temperature of dehydroxylation/decarbonation and decreasing temperature of desulfurization were observed at a smaller RE^{3+}. Phase-pure $RE_2O_2SO_4$ can be readily obtained from the hydroxide

compounds by calcination in air at 800 °C. The optimal Sm^{3+} content was determined to be ~1 at.% for the $Gd_2O_2SO_4$ host, and concentration quenching of luminescence was suggested to occur via electric dipole-dipole interaction. The $Gd_2O_2SO_4$:0.05Eu and $Gd_2O_2SO_4$:0.01Sm phosphors were analyzed to have fluorescence lifetimes of ~2.43 and 2.40 ms and be able to retain ~79.6 and 85.5% of the room-temperature intensity at 423 K for their 617 nm (λ_{ex} = 275 nm) and 608 nm (λ_{ex} = 407 nm) main emissions, respectively. Application in optical thermometry via the fluorescence intensity ratio technology indicated that the $Gd_2O_2SO_4$:0.05Eu phosphor has a maximum relative sensitivity (S_r) of ~2.70% K^{-1} at 298 K for the thermally coupled $^5D_0/^5D_1$ energy levels and for excitation under 325 nm (CTB edge)/395 nm ($^5F_0 \rightarrow 5L_6$ transition), while the $Gd_2O_2SO_4$:0.01Sm phosphor has a maximum S_r of ~1.73% K^{-1} at 298 K for excitation under 244 nm (CTB edge)/407 nm ($^6H_{5/2} \rightarrow {}^4K_{11/2}$ transition). The temperature resolution reached ~0.15 and 0.23 K for the *FIR*($^5D_1/^5D_0$) and *FIR*(I_{325}/I_{395}) of $Gd_2O_2SO_4$:0.05Eu and ~0.23 K for the *FIR*(I_{244}/I_{407}) of $Gd_2O_2SO_4$:0.01Sm at 298 K. Both the types of phosphors also showed good reversibility and repeatability for temperature sensing, whose repeatability factor is better than 98.7%.

Acknowledgements

This work was supported in part by the National Natural Science Foundation of China (Grant No. 52172112 and 51972047).

References

1. A. Kasten and G. Hess: Magnetic Properties of $Tb_2O_2SO_4$ *Phys. Status Solidi B.* **123**(1), 123 (1984).
2. H. Hülsing, H.G. Kahle, M. Schwab and H.J. Schwarzbauer: Specific heat of rare

earth oxisulphates ($RE_2O_2SO_4$) *J. Magn. Magn. Mater.* **9**(1), 68 (1978).
3. W. Paul: Magnetism and magnetic phase diagram of $Gd_2O_2SO_4$ I. Experiments *J. Magn. Magn. Mater.* **87**(1), 23 (1990).
4. M. Machida, K. Kawamura, K. Ito and K. Ikeue: Large-capacity oxygen storage by lanthanide oxysulfate/oxysulfide systems *Chem. Mater.* **17**(6), 1487 (2005).
5. K. Ikeue, M. Eto, D. Zhang, T. Kawano and M. Machida: Large-capacity oxygen storage of Pd-loaded $Pr_2O_2SO_4$ applied to anaerobic catalytic CO oxidation *J. Catal.* **248**(1), 46 (2007).
6. G. Chen, F. Chen, X. Liu, W. Ma, H. Luo, J. Li, R. Ma and G. Qiu: Hollow spherical rare-earth-doped yttrium oxysulfate: A novel structure for upconversion *Nano Res.* **7**(8), 1093 (2014).
7. L. Song, P. Du, Q. Jiang, H. Cao and J. Xiong: Synthesis and luminescence of high-brightness $Gd_2O_2SO_4:Tb^{3+}$ nanopieces and the enhanced luminescence by alkali metal ions co-doping *J. Lumin.* **150**, 50 (2014).
8. X. Wang, J.-G. Li, M.S. Molokeev, Q. Zhu, X. Li and X. Sun: Layered hydroxyl sulfate: Controlled crystallization, structure analysis, and green derivation of multi-color luminescent $(La,RE)_2O_2SO_4$ and $(La,RE)_2O_2S$ phosphors (RE = Pr, Sm, Eu, Tb, and Dy) *Chem. Eng. J.* **302**, 577 (2016).
9. R. Ballestracci and J. Mareschal: Etude structurale des sulfates basiques de terres rares et d'yttrium *Mater. Res. Bull.* **2**(11), 993 (1967).
10. S. Zhukov, A. Yatsenko, V. Chernyshev, V. Trunov, E. Tserkovnaya, O. Antson, J. Hölsä, P. Baulés and H. Schenk: Structural study of lanthanum oxysulfate $(LaO)_2SO_4$ *Mater. Res. Bull.* **32**(1), 43 (1997).
11. O. Siidra, D. Charkin, I. Plokhikh, E. Nazarchuk, A. Holzheid and G. Akimov: Expanding family of litharge-derived sulfate minerals and synthetic compounds: Preparation and crystal structures of $[Bi_2CuO_3]SO_4$ and $[Ln_2O_2]SO_4$ (Ln = Dy and Ho) *Miner.* **10**(10), 887 (2020).
12. R.V. Rodrigues, L. Marciniak, L.U. Khan, E.J.B. Muri, P.C.M. Cruz, J.R. Matos, W. Strek and A.A.L. Marins: Impact of Tb^{3+} ion concentration on the morphology, structure and photoluminescence of $Gd_2O_2SO_4:Tb^{3+}$ phosphor obtained using thermal decomposition of sulfate hydrate *Luminescence.* **35**(8), 1254 (2020).
13. M. Machida, K. Kawamura, T. Kawano, D. Zhang and K. Ikeue: Layered Pr-dodecyl sulfate mesophases as precursors of $Pr_2O_2SO_4$ having a large oxygen-storage capacity *J. Mater. Chem.* **16**(30), 3084 (2006).
14. T. Kijima, T. Isayama, M. Sekita, M. Uota and G. Sakai: Emission properties of Tb3+ in Y2O2SO4 derived from their precursory dodecylsulfate-templated concentric- and straight-layered nanostructures *J. Alloys Compd.* **485**(1), 730 (2009).
15. D. Ma, C. Li, L. Wang, H. Liu, S. Zhong and Y. Li: Preparation of RE2O2SO4 (RE=La, Pr-Lu) microspheres from rare-earth-based infinite coordination polymers *J. Nanopart. Res.* **19**(10), (2017).
16. F. Gándara, J. Perles, N. Snejko, M. Iglesias, B. Gómez-Lor, E. Gutiérrez-Puebla and M.Á. Monge: Layered rare-earth hydroxides: A class of pillared crystalline compounds for intercalation chemistry *Angew. Chem. Int. Ed.* . **45**(47), 7998 (2006).
17. J. Liang, R. Ma, F. Geng, Y. Ebina and T. Sasaki: $Ln_2(OH)_4SO_4 \cdot nH_2O$ (Ln = Pr to Tb;

n∼2): A new family of layered rare-earth hydroxides rigidly pillared by sulfate ions *Chem. Mater.* **22**(21), 6001 (2010).
18. X. Wang, M.S. Molokeev, Q. Zhu and J.-G. Li: Controlled hydrothermal crystallization of anhydrous $Ln_2(OH)_4SO_4$ (Ln=Eu–Lu, Y) as a new family of layered rare earth metal hydroxides *Chem. Eur. J.* **23**(63), 16034 (2017).
19. X. Wang, J.-G. Li, M.S. Molokeev, X. Wang, W. Liu, Q. Zhu, H. Tanaka, K. Suzuta, B.-N. Kim and Y. Sakka: Hydrothermal crystallization of a $Ln_2(OH)_4SO_4{\cdot}nH_2O$ layered compound for a wide range of Ln (Ln = La–Dy), thermolysis, and facile transformation into oxysulfate and oxysulfide phosphors *RSC Adv.* **7**(22), 13331 (2017).
20. F. Geng, R. Ma, Y. Matsushita, J. Liang, Y. Michiue and T. Sasaki: Structural study of a series of layered rare-earth hydroxide sulfates *Inorg. Chem.* **50**(14), 6667 (2011).
21. J.-G. Li, Q. Zhu, X. Li, X. Sun and Y. Sakka: Colloidal processing of Gd_2O_3:Eu^{3+} red phosphor monospheres of tunable sizes: Solvent effects on precipitation kinetics and photoluminescence properties of the oxides *Acta Mater.* **59**(9), 3688 (2011).
22. Z. Luo, F. Li, Q. Zhu, X. Sun and J.-G. Li: Low-temperature green synthesis of nanocrystalline La_2O_2S:Pr^{3+} powders and investigation of photoluminescence *J. Mater. Res. Technol.* **17**, 2540 (2022).
23. Z. Luo, F. Li, Q. Zhu, X. Li, X. Sun and J.-G. Li: Sulfidization-free synthesis of well dispersed $(Gd,La)_2O_2S$:Pr^{3+} nanopowders and the effect of La^{3+} on structure and luminescence *J. Mater. Res. Technol.* **18**, 4216 (2022).
24. F. Li, M. Jin, Z. Li, X. Wang, Q. Zhu and J.-G. Li: Vertically aligned $Gd_2O_2SO_4$:Ln and Gd_2O_2S:Ln luminescent films with super-hydrophobicity via a novel precursor route (Ln = Pr, Eu, Tb) *Appl. Surf. Sci.* **609**, 155323 (2023).
25. X. Wang, J.-G. Li, Q. Zhu and X. Sun: Photoluminescence of (La,Eu)2O2SO4 red-emitting phosphors derived from layered hydroxide *J. Mater. Res.* **31**(15), 2268 (2016).
26. P.W. Ayers: An elementary derivation of the hard/soft-acid/base principle *J. Chem. Phys.* **122**(14), 141102 (2005).
27. R.L. Rich: Inorganic reactions in water (Springer-Verlag, City, 2007).
28. M. Li and J.-G. Li: Extensive tailoring of $REPO_4$ and $REVO_4$ crystallites via solution processing and luminescence *CrystEngComm.* **24**(27), 4841 (2022).
29. J.A. Gadsden: Infrared spectra of minerals and related inorganic compounds (Butterworth, City, 1975).
30. F. Li, J.-G. Li and Q. Zhu: EDTA-promoted aliovalent Eu^{3+} doping of $Sr_5(PO_4)_3F$ apatite, growth behavior and luminescence *Opt. Mater.* **101**, 109765 (2020).
31. E.L. Head and C.E. Holley, Jr.: The preparation and thermal decomposition of some rare earth carbonates, in In Rare Earth Research II, City, 1964).
32. E.L. Head and C.E. Holley, Jr.: The preparation and thermal decomposition of the carbonates of Tb, Dy, Ho, Er, Tm, Yb, Lu, Y, and Sc, in In Rare Earth Research, City, 1965).
33. R.D. Shannon: Revised effective ionic radii and systematic studies of interatomie distances in halides and chaleogenides *Acta Crystallogr.* **A**(32), 751 (1976).
34. Y. Sun, H. Zou, B. Zhang, X. Zhou, Y. Song, K. Zheng, Z. Shi and Y. Sheng:

Luminescent properties and energy transfer of Gd^{3+}/Eu^{3+} co-doped cubic $CaCO_3$ *J. Lumin.* **178**, 307 (2016).

35. J.-G. Li, X. Li, X. Sun and T. Ishigaki: Monodispersed Colloidal Spheres for Uniform $Y_2O_3:Eu^{3+}$ Red-Phosphor Particles and Greatly Enhanced Luminescence by Simultaneous Gd^{3+} Doping *J. Phys. Chem. C.* **112**(31), 11707 (2008).
36. C.-J. Duan, W.-F. Li, X.-Y. Wu, H.-H. Chen, X.-X. Yang, J.-T. Zhao, Y.-B. Fu, Z.-M. Qi, G.-B. Zhang and Z.-S. Shi: Photoluminescence of Ce^{3+}, Tb^{3+}, Sm^{3+} or Gd^{3+} activated $Ba_3BP_3O_{12}$ under the VUV and UV excitation *Mater. Sci. Eng. B.* **121**(3), 272 (2005).
37. K.R. Kalimuthu, S. Moorthy Babu and V. Kalimuthu: Synthesis and photoluminescence properties of Sm^{3+} doped $LiGd(WO_4)_2$ phosphors with high color purity *Opt. Mater.* **102**, 109804 (2020).
38. S. Huang and L. Lou: Concentration dependence of sensitizer fluorescence intensity in energy transfer *Chin. J. Lumin.* **11**(1), 36 (1990).
39. G. Blasse: Energy transfer between inequivalent Eu^{2+} ions *J. Solid State Chem.* **62**(2), 207 (1986).
40. Z. Xu, Q. Zhu, X. Li, X. Sun and J.-G. Li: Systematic crystallization of $NH_4Ln(MoO_4)_2$ as a family of layered compounds (Ln = La-Lu and Y), derivation of $Ln_2Mo_4O_{15}$, crystal structure, and photoluminescence *Inorg. Chem.* **61**(38), 15116 (2022).
41. S. Zhou, C. Duan and M. Wang: Origin of the temperature-induced redshift of the charge transfer band of $GdVO_4$ *Opt. Lett.* **42**(22), 4703 (2017).
42. S. Zhou, C. Duan and S. Han: A novel strategy for thermometry based on the temperature-induced red shift of the charge transfer band edge *Dalton Trans.* **47**(5), 1599 (2018).
43. X. Wang, Q. Liu, Y. Bu, C.-S. Liu, T. Liu and X. Yan: Optical temperature sensing of rare-earth ion doped phosphors *RSC Adv.* **5**(105), 86219 (2015).
44. C. Wang, Y. Jin, R. Zhang, Q. Yao and Y. Hu: A review and outlook of ratiometric optical thermometer based on thermally coupled levels and non-thermally coupled levels *J. Alloys Compd.* **894**, 162494 (2022).
45. I.E. Kolesnikov, M.A. Kurochkin, E.V. Golyeva, D.V. Mamonova, A.A. Kalinichev, E.Y. Kolesnikov and E. Lahderanta: Multimode high-sensitivity optical $YVO_4:Ln^{3+}$ nanothermometers (Ln^{3+} = Eu^{3+}, Dy^{3+}, Sm^{3+}) using charge transfer band features *Phys. Chem. Chem. Phys.* **22**(48), 28183 (2020).
46. M. Jia, Z. Sun, M. Zhang, H. Xu and Z. Fu: What determines the performance of lanthanide-based ratiometric nanothermometers? *Nanoscale.* **12**(40), 20776 (2020).
47. V.K. Rai: Temperature sensors and optical sensors *Appl. Phys. B.* **88**(2), 297 (2007).
48. K.W. Meert, V.A. Morozov, A.M. Abakumov, J. Hadermann, D. Poelman and P.F. Smet: Energy transfer in Eu^{3+} doped scheelites: use as thermographic phosphor *Opt. Express.* **22**(S3), A961 (2014).
49. M.G. Nikolić, D.J. Jovanović and M.D. Dramićanin: Temperature dependence of emission and lifetime in Eu^{3+}- and Dy^{3+}-doped $GdVO_4$ *Appl. Opt.* **52**(8), 1716 (2013).
50. L. Zhao, Z. Cao, X. Wei, M. Yin and Y. Chen: Luminescence properties of Eu^{3+} doped YBO_3 for temperature sensing *J. Rare Earths.* **35**(4), 356 (2017).

51. X. Zhou, S. Zhao, S. Li, Y. Wang, L. Li, S. Jiang, G. Xiang, C. Jing, J. Li and L. Yao: Luminescent properties of Eu^{3+}-doped $NaLaCaWO_6$ red phosphors and temperature sensing derived from the excited state of charge transfer band *J. Lumin.* **248**, 118964 (2022).
52. S. Zhou, C. Duan, M. Yin, S. Zhang and C. Wang: High-sensitive optical temperature sensing based on $^5D_1$ emission of Eu^{3+} in YVO_4 *J. Alloys Compd.* **784**, 970 (2019).
53. C. Han, X. Li, Y. Duan, R. Shen, L. Cheng, Z. Guan, S. Xu, J. Sun, H. Yu and B. Chen: Photoluminescence, optical transition properties and temperature-induced shift of charge transfer band and temperature sensing property of $GdNbTiO_6$: Sm^{3+} phosphors *Spectrochim. Acta, Part A.* **260**, 119951 (2021).
54. Y. Hua, J.-U. Kim and J.S. Yu: Charge transfer band excitation of La_3NbO_7:Sm^{3+} phosphors induced abnormal thermal quenching toward high-sensitivity thermometers *J. Am. Ceram. Soc.* **104**(8), 4065 (2021).
55. P. Du, X. Sun, Q. Zhu and J.-G. Li: Garnet-structured $Li_6CaLa_2Nb_2O_{12}$:Yb/Er new phosphor showing superior performance of optical thermometry *Scr. Mater.* **185**, 140 (2020).
56. W. Liu, X. Wang, Q. Zhu, X. Li, X. Sun and J.-G. Li: Upconversion luminescence and favorable temperature sensing performance of eulytite-type $Sr_3Y(PO_4)_3$:Yb^{3+}/Ln^{3+} phosphors (Ln=Ho, Er, Tm) *Sci. Technol. Adv. Mat.* **20**(1), 949 (2019).
57. K. Zheng, W. Song, G. He, Z. Yuan and W. Qin: Five-photon UV upconversion emissions of Er^{3+} for temperature sensing *Opt. Express.* **23**(6), 7653 (2015).
58. F. Huang, T. Yang, S. Wang, L. Lin, T. Hu and D. Chen: Temperature sensitive cross relaxation between Er^{3+} ions in laminated hosts: a novel mechanism for thermochromic upconversion and high performance thermometry *J. Mater. Chem. C.* **6**(45), 12364 (2018).
59. T. Zheng, M. Runowski, N. Stopikowska, M. Skwierczyńska, S. Lis, P. Du and L. Luo: Dual-center thermochromic Bi_2MoO_6:Yb^{3+},Er^{3+},Tm^{3+} phosphors for ultrasensitive luminescence thermometry *J. Alloys Compd.* **890**, 161830 (2022).
60. C. Mi, J. Zhou, F. Wang, G. Lin and D. Jin: Ultrasensitive ratiometric nanothermometer with large dynamic range and photostability *Chem. Mater.* **31**(22), 9480 (2019).
61. M. Dai, Z. Fu, Z. Wang and H. Xu: Sc^{3+}-induced double optimization strategies for boosting NIR-II luminescence and improving thermometer performance in CaF_2:Nd^{3+}, Nd^{3+}/Yb^{3+}@$NaYF_4$ nanocrystals *Chem. Eng. J.* **452**, 139133 (2023).